

X-Ray Beaming due to Resonance Scattering in the Accretion Column of Magnetic Cataclysmic Variables

Y. Terada,¹ M. Ishida,² K. Makishima,¹ T. Imanari,³
R. Fujimoto,⁴ K. Matsuzaki,⁴ H. Kaneda⁴

¹ Department of Physics, Science, The University of Tokyo

² Department of Physics, Tokyo Metropolitan University

³ Engineering, The University of Tokyo

⁴ The Institute of Space and Astronautical Science

Accepted 2001 July 25; Received 2001 January 20; in original form 2001 May 08

ABSTRACT

Extremely strong ionized Fe emission lines, with the equivalent width reaching about 4000 eV, were discovered with ASCA from a few Galactic compact objects, including AX J2315–0592, RX J1802.1+1804 and AX J1842.8–0423. These objects are thought to be binary systems containing magnetized white dwarfs (WDs). A possible interpretation of the strong Fe-K line is the line-photon collimation in the WD accretion column, due to resonance scattering of line photons. The collimation occurs when the accretion column has a flat shape, and the effect is augmented by the vertical velocity gradient there, which reduces the resonant trapping of resonant photons along the magnetic field lines. This effect was quantitatively confirmed with Monte-Carlo simulations. Furthermore, with ASCA observations of the polar V834 Centauri, this collimation effect was clearly detected as a rotational modulation of the equivalent width of the Fe-K emission line. Extremely strong emission lines mentioned above can be explained by our interpretation consistently. Combing this effect with other X-ray information, the geometry and plasma parameters in the accretion column were determined.

Key words: radiation mechanisms: thermal – scattering – X-rays: stars – stars: white dwarfs – stars: individual: (V834 Cen) – methods: observation

1 INTRODUCTION

A polar (or AM Her type object) is a binary system consisting of a low-mass main sequence star filling its Roche lobe and a magnetized white dwarf (WD) with 10^{7-8} G magnetic field, which is strong enough to lock the WD spin with the orbital motion. Matter spilling over the Roche lobe of the companion star is captured by the magnetic field of the WD and accretes onto its magnetic poles, emitting hard X-rays via optically-thin thermal bremsstrahlung.

Extremely strong ionized iron emission lines have been discovered from a few polars with the X-ray observation by ASCA. For example, AX J2315–0592 has a strong ionized Fe-K α line centered at $6.84^{+0.13}_{-0.09}$ keV, whose equivalent width (EW) reaches 900^{+300}_{-200} eV (Misaki et. al 1996), and RX J1802.1+1804 has a strong Fe-K α line with EW ~ 4000 eV (Ishida et. al 1998). To interpret these strong line emissions as thermal plasma emission, the plasma metallicity needs to much exceed one solar abundance; ~ 2 solar for AX J2315–0592, and 3.04 ± 1.47 solar for RX J1802.1+1804. Although WD binaries often exhibit highly ionized Fe-K

lines, the implied abundances are usually sub-solar, such as $0.4^{+0.2}_{-0.1}$ solar for AM Her (Ishida et al. 1997), 0.63 ± 0.08 solar for EX Hya (Fujimoto, Ishida 1997), and ~ 0.4 solar for SS Cyg (Done, Osborne 1997). Therefore, we speculate that the unusually high iron abundances of the present two WD binaries result from some mechanisms to enhance the line EW, rather than from high metallicities of the mass-donating stars.

We find a common feature in these two object, which may provide a clue to the strong iron K line. AX J2315–0592 exhibits a large ($87 \pm 2\%$, $57 \pm 2\%$) orbital modulation in the 0.7 – 2.3 keV and 2.3 – 6.0 keV light curves, but almost no modulation in the 6.0 – 10.0 keV band. Similarly, RX J1802.1+1804 exhibits a large ($\sim 100\%$) orbital modulation amplitude below 0.5 keV with ROSAT observation (Greiner et al. 1998), but the ASCA light curves are extremely flat (Ishida et al. 1998). The lack of hard-band modulation implies that a constant fractional volume of the accretion columns (which are optically thin to continuum X-rays) is observed throughout the rotational phase, and hence the inclination of the orbital plane i is rather small.

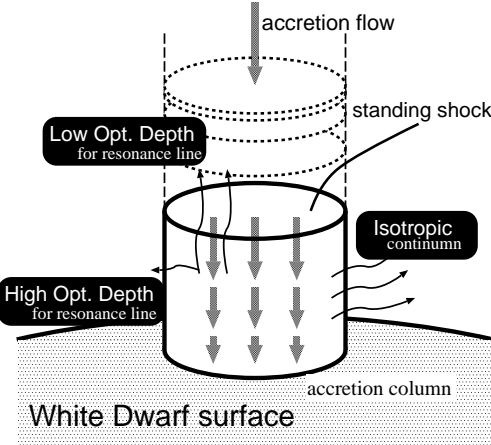


Figure 1. Schematic view of an accretion column on the WD in a polar system

Then, the soft-band modulation must be due to changes in absorption by the pre-shock accretion flow, indicating that we observe down onto a single pole at the absorption maximum. This in turn requires the magnetic co-latitude β to be close to i . In short, these systems are inferred to have $\beta \sim i \sim 0$. In this paper, we call such a polars as ‘‘POLE (Pole-On Line Emitter)’’.

We have another example of extremely strong iron K line emitter, an X-ray transient source AX J1842–0423, discovered with ASCA in 1996 October on the Galactic plane in the Scutum arm region (Terada et al. 1999; hereafter paper I). The most outstanding feature of this object revealed by the ASCA GIS is the very conspicuous emission line at $6.78^{+0.10}_{-0.13}$ keV, whose EW is extremely large at 4000^{+1000}_{-500} eV. To explain this line EW, a plasma metallicity as high as $3.0^{+4.3}_{-0.9}$ solar abundance would be required. We found no periodicity over the period range of 62.5 ms to a few hours, the latter being a typical orbital period of polars. In view of the thin-thermal spectrum and the allowed source size of $10^{8.5-17.7}$ cm, we have concluded in paper I that AX J1842–0423 is likely to another POLE, like AX J2315–0592 or RX J1802.1+1804.

The face-value metallicities of the three objects are so high that we regard these values to be unrealistic. Instead, we consider that the iron K line EW is much enhanced by some mechanism, which may be common to the POLEs. To account for the strong iron K line of three POLEs, the mechanism must account for line enhancement by a factor of 3 or more. In this paper, we develop the possible explanation invoking resonance scattering (§2), which has been proposed briefly in paper I. In the present paper, we carry out Monte-Carlo simulations (§3) to confirm the proposed mechanism, and verify the effect through ASCA observations of the polar V834 Cen (§4).

2 LINE ENHANCEMENT DUE TO RESONANCE PHOTON BEAMING

2.1 Geometrical beaming of Fe resonance line

In a polar system, a flow of matter accreting onto each magnetic pole of the WD is highly supersonic, so that a stand-

ing shock is formed close to the WD. The matter is shock heated up to a temperature k of a few tens keV [Appendix A equation (A1)]. The heated plasma cools by radiating Bremsstrahlung hard X-ray continuum and line photons, as it flows down the column, to form a hot accretion column of height h and radius r as illustrated in figure 1. We can assume that the ion temperature is equal to the electron temperature, because the ion to electron energy transfer time scale t_{eq} is much shorter than the cooling time scale $t_{\text{ff,cool}}$ [Appendix A, equations (A7) and (A6)].

The typical accretion rate of polars is $\dot{M} \sim 10^{16}$ g s $^{-1}$, r is typically 5×10^7 cm, and the velocity immediately beneath the shock front is typically $u^{\text{sh}} \sim 10^8$ cm s $^{-1}$ [Appendix A equation (A2)], so that the electron density at the top of the hot accretion column is typically $n_e^{\text{sh}} \sim 10^{15-16}$ cm $^{-3}$ [Appendix A equation (A3)]. The optical depth of the column for Thomson scattering is then given by

$$\tau_T = 0.24 \left(\frac{r}{5 \times 10^7 \text{ cm}} \right) \left(\frac{n_e^{\text{sh}}}{7.7 \times 10^{15} \text{ cm}^{-3}} \right), \quad (1)$$

and the optical depth of free-free absorption is much smaller [Appendix A equation (A8)]. Therefore, the column is optically thin for both electron scattering and free-free absorption, so the continuum X-rays are emitted isotropically.

On the other hand, the optical depth for the resonance scattering is calculated from equation (A10) in Appendix A as

$$\tau_R = 36 \left(\frac{n_e}{7.7 \times 10^{15} \text{ cm}^{-3}} \right) \left(\frac{A_{\text{Fe}}}{4.68 \times 10^{-5}} \right) \left(\frac{r}{5 \times 10^7 \text{ cm}} \right), \quad (2)$$

at the energy of the hydrogenic iron K_{α} line, where A_{Fe} is the abundance of iron by number, which is normalized to the value of one solar. Thus, the accretion column is optically thick for resonance lines, and the resonance line photons can only escape from positions close to the surface of accretion column. If the accretion column has a flat coin-shaped geometry, and our line-of-sight is nearly pole-on to it, we will observe the enhanced Fe-K lines. We call this effect ‘‘geometrical beaming’’. However, this effect can explain the Fe-K line enhancement up to a factor of 2.0 [Appendix B], which is insufficient to explain the factor ~ 3 enhancements observed from POLEs. An additional mechanism is clearly needed.

2.2 Additional collimation by vertical velocity gradient

In the accretion column of a polar, both temperature kT and u decrease, and n_e increases from the shock front toward the WD surface. Numerically, the vertical profiles of these quantities are calculated by Aizu (1973), as a function of vertical distance z from the WD surface, as equation (A4) in Appendix A. Because of Doppler shift caused by this strong vertical velocity gradient in the post-shock flow, the resonance line energy changes continuously in the vertical direction. Let us consider, for example, that a line photon of rest-frame energy E_0 is produced near the bottom of accretion column, $z \simeq 0.1h$, where the emissivity of He-like iron line photon becomes maximum, and that this photon moves vertically by its mean free path of resonance scattering l_R which is given as

$$l_R = (\sigma_R A_{\text{Fe}} n_e)^{-1}$$

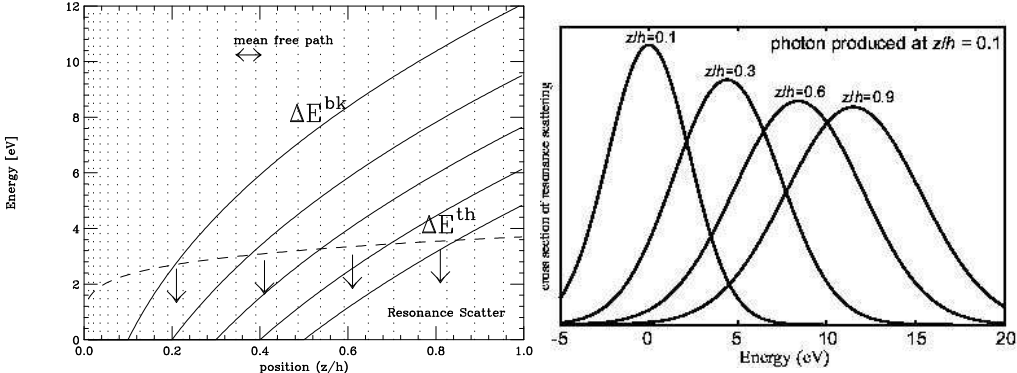


Figure 2. (left) The cumulative shift of the resonance energy (solid line) for upward-moving Fe-K line photons, which are produced at $z = 0.1h, 0.2h, 0.3h, 0.4h$, and $0.5h$. The thermal width of the resonant Fe-K line is given by the dashed curve. Separations of the adjacent dotted vertical lines specify the mean free path l_R of resonant photons. (right) Cross section of resonance scattering for an iron K_α line photon, which is produced at $z/h = 0.10$ and moves vertically. The resonance centroid energy corresponds to ΔE^{bk} shown in the left panel, and the resonance energy width corresponds to ΔE^{th} .

$$= 1.3 \times 10^6 \left(\frac{z}{h}\right)^{\frac{2}{5}} \left(\frac{n_e^{sh}}{7.7 \times 10^{15} \text{ cm}^{-3}}\right)^{-1} \times \left(\frac{A_{Fe}}{4.68 \times 10^{-5}}\right) \text{ cm.} \quad (3)$$

Because h is given as equation (A5) [Appendix A], l_R is roughly equal to $0.07h(\frac{z}{h})^{2/5}$. Over this distance along the z -direction, u will change by $\Delta u = 4.0 \times 10^6 \text{ cm s}^{-1}$ at $z \simeq 0.1h$ from equation (A4), so the resonance energy for the line photon shifts due to Doppler effect over the same distance by

$$\Delta E^{bk} = E_0 \frac{\Delta u}{c} = 0.9 \left(\frac{E_0}{6.695 \text{ keV}}\right) \left(\frac{u^{sh}}{0.9 \times 10^8 \text{ cm}^{-3}}\right) \text{ eV,} \quad (4)$$

where c is the light velocity. Figure 2 shows the change of ΔE^{bk} for upward-moving photons produced at various depths of the accretion column.

The width ΔE of the resonance scattering [see Appendix A equation (A9)] is determined by the natural width of line photon ($\sim 1 \text{ eV}$ for iron K ion) and by the thermal Doppler broadening ΔE^{th} . Because the thermal velocity of ion of mass m_i reaches

$$v_i = \sqrt{\frac{kT^{sh}}{m_i}} = 2.4 \times 10^7 \left(\frac{z}{h}\right)^{\frac{1}{5}} \left(\frac{m_i}{56m_H}\right)^{-\frac{1}{2}} \left(\frac{kT^{sh}}{16 \text{ keV}}\right)^{\frac{1}{2}} \text{ cm s}^{-1} \quad (5)$$

with m_H the mass of a hydrogen atom, the thermal Doppler width of the resonance becomes

$$\Delta E^{th}(z) = E_0 \cdot \frac{v_i}{c} = 3.7 \left(\frac{z}{h}\right)^{\frac{1}{5}} \left(\frac{m_i}{56m_H}\right)^{-\frac{1}{2}} \times \left(\frac{E_0}{6.695 \text{ keV}}\right) \left(\frac{kT^{sh}}{16 \text{ keV}}\right)^{\frac{1}{2}} \text{ eV.} \quad (6)$$

Here we normalized the equation to the iron atom, $m_i = 56m_H$. The dashed line in figure 2 shows the position depen-

dence of ΔE^{th} , below which the resonance scattering does occur.

Figure 2 clearly shows that, if a line photon gradually moves upward through repeated scattering, its energy becomes different from the local resonance energy, by an amount ΔE^{bk} [equation (4)] which eventually becomes larger than the thermal width ΔE^{th} [equation (6)]. Numerically, this ratio for a photon produced at $z = z_0$ can be described as

$$\frac{\Delta E^{bk}(z)}{\Delta E^{th}(z)} = \frac{\Delta u}{v_i} = \frac{u^{sh} \left\{ (z/h)^{\frac{2}{5}} - (z_0/h)^{\frac{2}{5}} \right\}}{\sqrt{3 \frac{\mu m_H}{m_i} u^{sh} \left(\frac{z}{h}\right)^{\frac{1}{5}}}} = 5.5 \left(\frac{m_i}{56m_H}\right)^{\frac{1}{2}} \left(\frac{\mu}{0.615}\right) \times \left\{ \left(\frac{z}{h}\right)^{\frac{1}{5}} - \left(\frac{z_0}{h}\right)^{\frac{2}{5}} \left(\frac{z}{h}\right)^{-\frac{1}{5}} \right\} \quad (7)$$

$$\simeq 2.2 \left(\frac{m_i}{56m_H}\right)^{\frac{1}{2}} \left(\frac{\mu}{0.615}\right) \times \left(\frac{\delta z}{h}\right) \left(\frac{z}{h}\right)^{-\frac{4}{5}} [\delta z \ll h], \quad (8)$$

where $\delta z = z - z_0$, and μ is the mean molecular weight ($\mu = 0.615$ for a plasma of one-solar abundance), and we used the relation of $kT^{sh} = 3\mu m_H \cdot (u^{sh})^2$ from equations (A1) and (A2). Then, the photon is no longer scattered efficiently, and can escape out. This effect does not occur in the horizontal direction because of little velocity gradient. As a result, a resonant line photon produced near bottom of the accretion column thus escapes with a higher probability when its net displacement due to random walk is directed upward, rather than horizontal. In other words, iron K line photons are collimated to the vertical direction. We call this effect “velocity gradient beaming”. The essence of this effect is that the mass of iron, m_i in equation (7), is heavy enough for the bulk velocity gradient to overcome the thermal line broadening.

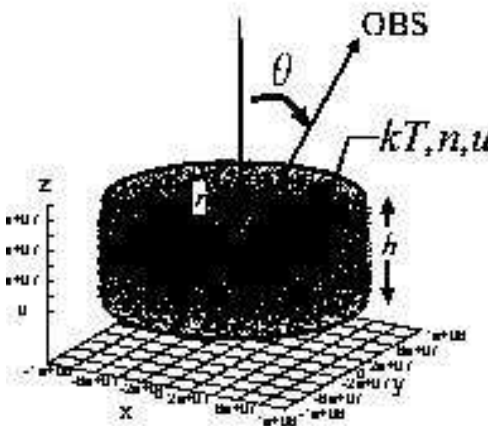


Figure 3. Definition of the cylinder in our simulation.

3 MONTE-CARLO SIMULATION

The collimation effect described in section 2 involves significant scattering processes, which make analytic calculation difficult. In this section, we accordingly examine the proposed effect using Monte-Carlo simulations.

3.1 overview of the simulation

Consider a simple cylinder of height h and radius r , filled with X-ray emitting plasma. We describe the vertical dependence of kT , n_e , and u in the cylinder by equation (A4). We then produce a number of Monte-Carlo iron line photons in proportion to its emissivity, which in turn is determined by kT and n_e there. We isotropically randomize their initial direction of propagation in the rest frame of iron nuclei. The line energy of each iron photon is also randomized; i.e. the average value of the energy is Doppler shifted in the frame of observers according to the bulk velocity law [eq. (4)], and its dispersion is determined by the local thermal motion [eq. (5)]. We trace the propagation of each line photon with a constant step length, which is taken to be 1/100 of the mean free path of resonance scattering at the bottom of the cylinder, where the temperature falls below 1 keV. At each step, the behavior of photon is determined by the calculated probabilities of resonance scattering and Compton scattering. We follow the propagation of each photon until it moves outside the cylinder.

3.2 basic condition

The temperature dependence of iron line emissivity in optically thin plasma has been calculated by many authors, and we here adopt the calculation by Mewe et al. (1985) as shown in figure 4. We consider four species of iron K line photons; those of H-like resonance K_α line (6.965 keV), He-like resonance K_α line (6.698 keV), He-like intercombination line (6.673 keV), and He-like forbidden line (6.634 keV). The emissivity of iron line photons per unit volume, in $\text{erg s}^{-1} \text{cm}^{-3}$, is described for each species as

$$P = P'(kT) \cdot n_e n_{\text{Fe}}, \quad (9)$$

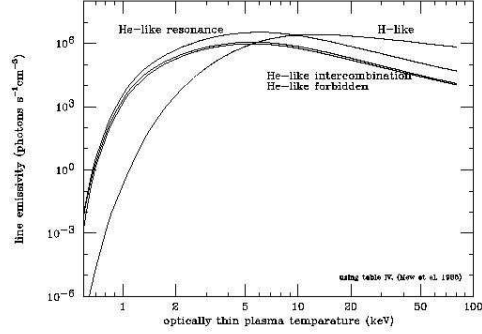


Figure 4. Temperature dependence of the Fe line emissivity (Mewe et al. 1985) adopted in the calculation.

where $P'(kT)$ in $\text{erg s}^{-1} \text{cm}^{-3}$ is the value shown in figure 4. The iron density n_{Fe} , in cm^{-3} , is calculated assuming one solar abundance. The position dependence of iron line emissivity is determined, through equation (9), by the z dependence of kT and n_{Fe} [equation (A4)].

Treatment of the resonance scattering process, taking into account both the bulk flow and the thermal motion of ions, is a key point of the present simulation. For each line photon being traced, its scattering probability at the i -th step \vec{r}_i is calculated as $\propto n_{\text{Fe}}(\vec{r}_i) \sigma_{\text{RS}}(E_i^{\text{in}})$, where $n_{\text{Fe}}(\vec{r}_i)$ is the local Fe-ion density at the position \vec{r}_i [see Appendix A equations (A3) and (A4)], σ_{RS} is the cross section for the resonance scattering given by eq. (A9)[Appendix A], and E_i^{in} is the Doppler-shifted energy of the incoming photon measured in the rest frame of a representative Fe-ion at \vec{r}_i . The velocity \vec{w}_i of this Fe-ion, relative to the observer, is expressed as a sum of the bulk flow velocity u at \vec{r}_i , and a random thermal velocity v . We specifically calculate as

$$E_i^{\text{in}} = E_{i-1}^{\text{out}} \{1 + (\vec{w}_{i-1} - \vec{w}_i) \cdot \vec{e}_{i-1,i}/c\}, \quad (10)$$

where \vec{w}_{i-1} is the observer-frame velocity (bulk plus random) of the Fe-ion that scattered the line photon last time, E_{i-1}^{out} is the outgoing photon energy as expressed in the rest frame of the previous scatterer, $\vec{e}_{i-1,i}$ is the unit vector along the photon propagation direction from the $(i-1)$ -th to the i -th scattering site [figure 6]. If the scattering occurs at \vec{r}_i , we randomize the line photon energy from E_i^{in} to E_i^{out} according to the natural width, and isotropically randomize the direction of the outgoing photon, both in the rest frame of the present scatterer. If, instead, the scattering does not occur at \vec{r}_i , we proceed to the next step without changing its direction. Thus, our calculation automatically includes both the bulk-flow Doppler effect and the thermal broadening. However, we do not consider energy shifts by the ion recoil, which is completely negligible. The scattering probability for a non-resonant photon is set to 0.

In addition to the resonance scattering, we must consider the Compton scattering process; the energy E is shifted to $E/\{1 + \frac{E}{m_e c^2} (1 - \cos \theta_{\text{CMP}})\}$, where θ_{CMP} is the Compton scattering angle. For an iron K_α photon with energy $E \sim 6.8$ keV, a Compton scattering with $\theta_{\text{CMP}} \geq 10^\circ$ will change the photon energy beyond the resonance energy width of a few eV: then the resonance scattering can no longer occur after a large-angle Compton scattering. We take this effect into account in our simulation, using the probability distribu-

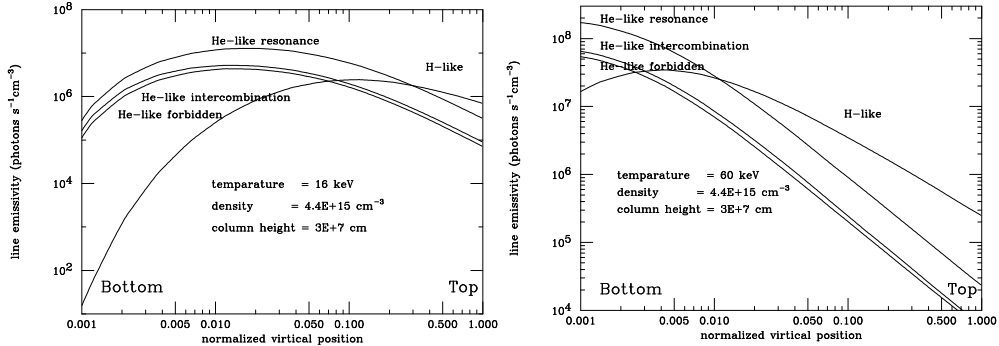


Figure 5. The volume emissivity of Fe-K line photons in the assumed accretion column, shown as a function of z/h . The plasma temperature is $kT^{\text{sh}} = 16$ keV (left panel), and 60 keV (right panel).

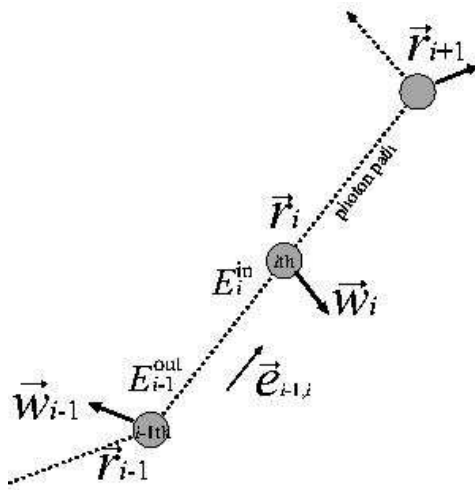


Figure 6. Schematic illustration of each step in our calculation; \vec{r}_i is the calculation site of i -th step, \vec{w}_i is the ion motion there in the observer's frame, which is a sum of bulk flow motion and random thermal motion, and E_i is the photon energy in the rest frame of i -th ion (See the text).

tion of θ_{CMP} by the Klein-Nishina formula, which is almost identical to the classical formula for the energy of iron lines. The differential scattering cross section and the energies of scattered photons are calculated in the rest frame of the currently scattering electron, so that the anisotropic effects caused by the bulk motion of electron is also included. Note that we neglect the process that the energy of a Compton-scattered continuum photon comes accidentally into the resonance energy range, since we do not generate continuum photons in the Monte-Carlo simulation.

3.3 results

First we simulated the simplest case wherein the plasma is hydrostatic with a single temperature and a single density: i.e. u is set to 0 and there is no vertical gradient in kT or n_e . The angular distributions of line photon flux, calculated under this simple condition for various densities, are shown in figure 7. The results confirm that the photons are emitted isotropically when the plasma density is low, but as the density increases, the geometrical beaming becomes progressively prominent. At $n_e = 10^{16-17} \text{ cm}^{-3}$, the Monte-Carlo

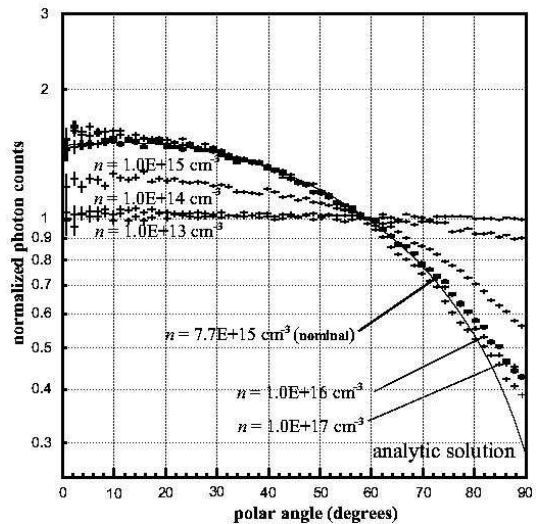


Figure 7. Angular distributions of resonant line photons emergent from a simple thin thermal plasma, simulated by neglecting the vertical motion ($u = 0$) and neglecting the vertical gradient in n and kT . Abscissa is the angle θ defined in figure 3, and ordinate is the photon flux per unit steradian normalized to the value of an isotropic emission. The plasma parameters are set to the nominal values; $kT = 16$ keV, $r = 5 \times 10^7$ cm, and $h = 1.9 \times 10^7$ cm. The solid line represents the analytic solution when only the column surface shines (equation B1). The crosses show the calculated results for various densities as given in the figure.

result agrees nicely with the analytic solution which assumes a completely optically-thick condition; i.e. line photons emit only from the surface of the accretion column [equation (B1); see Appendix B]. This verifies proper performance of our Monte-Carlo simulation.

Next we have fully considered the vertical gradient in kT , u , and n_e [eq. (A4)]. Figure 8 shows the calculated angular distribution of He-like iron line when the relevant parameters are set to the nominal values in equations (A1), (A2), and (A3). The resonance line flux is thus enhanced in the vertical direction more strongly than in figure 7. This reconfirms the physical beaming mechanism we proposed in § 2. The Compton scattering is confirmed to reduce the collimation only slightly. Finally, the intercombination photons, which are free from the resonance scattering, exhibit a nearly isotropic distribution.

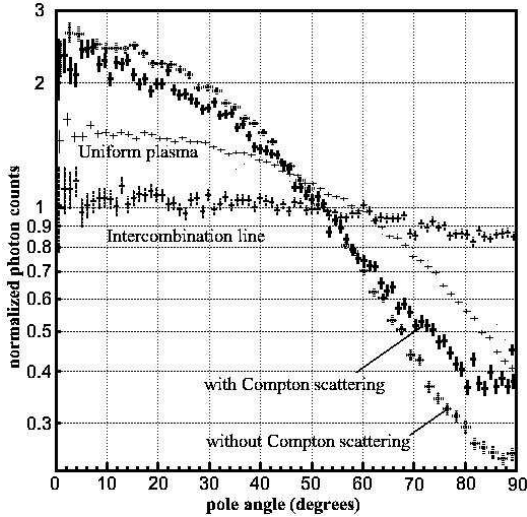


Figure 8. The same as figure 7, but calculated for the He-like iron K_{α} lines considering the vertical structure of the accretion column. The plasma parameters are set to the nominal values given in appendix A: $kT^{\text{sh}} = 16$ keV, $u^{\text{sh}} = 0.9 \times 10^8$ cm s $^{-1}$, $n_e^{\text{sh}} = 7.7 \times 10^{15}$ cm $^{-3}$, $r = 5 \times 10^7$ cm, and $h = 1.9 \times 10^7$ cm. Thick solid crosses represent the results considering the Compton scattering, while dashed crosses represent those neglecting the Compton process. The dotted crosses show the profile of the intercombination line. The thin crosses show the same profile as presented in figure 7 (nominal case).

We repeated the Monte-Carlo simulations by changing h/r , n_e^{sh} , kT , and u^{sh} , around their baseline values of $kT = 16.0$ keV, $u^{\text{sh}} = 0.9 \times 10^8$ cm s $^{-1}$, $n_e^{\text{sh}} = 7.7 \times 10^{15}$ cm $^{-3}$, $r = 5 \times 10^7$ cm, and $h = 1.9 \times 10^7$ cm (Appendix A). Figure 10 summarizes the obtained results in terms of the beaming factor

$$\xi_m = \frac{f(0)}{\int_0^{\pi/2} f(\theta) d\cos\theta} \quad (11)$$

where $f(\theta)$ is the angular distribution of line photon flux, such as is shown in figure 8. The beaming factor ξ_m increases as h/r decreases (i.e. coin shaped column), or density increases (figures 10a and b). However, when the density exceeds $\sim 10^{16}$ cm $^{-3}$, the beaming effect diminishes again, because of large-angle Compton scattering. This inference is achieved by comparing results with and without Compton process (figure 10b). The WD mass dependence of ξ_m is small (figure 9): it increases slightly with mass increases because shock velocity increases with deeper gravity potential, and it starts decreasing because density decreases. These results show clearly that the strong collimation of He-like iron K_{α} photons, with $\xi_m \geq 2$, is possible under reasonable conditions.

4 AN OBSERVATIONAL APPROACH

In order to experimentally verify our interpretation, it is necessary to measure the equivalent width of the resonant Fe-K lines as a function of viewing angle. For that purpose, we may utilize a polar of which our line-of-sight relative to the magnetic axis changes from $\sim 0^\circ$ (pole-on) to $\sim 90^\circ$ (side-on), as the WD rotates. Among the polars with well

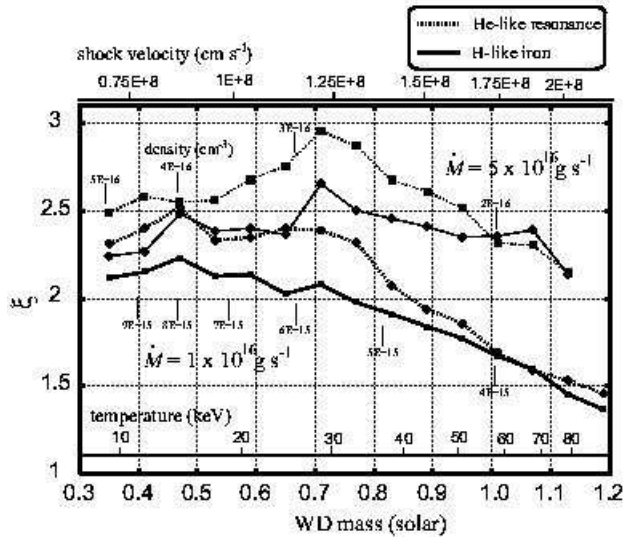


Figure 9. The beaming factor ξ_m with various WD mass. The H-like iron line is represented by solid lines and the He-like iron resonance line by dashed lines. The baseline condition is given in the text, and the temperatures and the densities change with WD mass and WE radius as shown in equations (A1) and (A2). The accretion rate to WD \dot{M} for calculation is set to 1×10^{16} g s $^{-1}$ and 5×10^{16} g s $^{-1}$.

determined system geometry (via optical, ultraviolet and infrared observations), V834 Cen is particularly suited: its orbital plane is inclined to our line-of-sight by $i = 45 \pm 9^\circ$, and its magnetic co-latitude is $\beta = 25 \pm 5^\circ$ (Cropper 1990). As a result, our line-of-sight to the accretion column changes from 20° to 70° .

4.1 observations of V834 Cen with ASCA

ASCA has four X-ray Telescopes (XRT: Selemitsos et al. 1995), and its common focal plane is equipped with two Gas Imaging Spectrometers (GIS: Ohashi et al. 1996; Makishima et al. 1996) and two Solid-state Imaging Spectrometers (SIS: Burke et al. 1991; Yamashita et al. 1997). The ASCA observation of V834 Cen was carried out for about 20 ksec from 1994 March 3.63 to 1994 March 4.13 (UT), and about 60 ksec from 1999 February 9.93 to 1999 February 10.72 (UT). In these observations, the GIS was operated in PH-nominal mode, which yields 0.7–10.0 keV X-ray spectra in 1024 channels, and the SIS was operated in 1-CCD FAINT mode, which produces 0.4–10.0 keV spectra in 4096 channels. The target was detected with a mean count rate of 0.171 c s $^{-1}$ per GIS detector and 0.259 c s $^{-1}$ per SIS detector in 1994. The corresponding count rates were 0.191 c s $^{-1}$ and 0.253 c s $^{-1}$ in 1999.

For extracting the source photons, we accumulated the GIS and SIS events within a circle of radius 45' centered on V834 Cen, employing the following data-selection criteria. We discarded the data during the ASCA passing through the South Atlantic Anomaly. We rejected the events acquired when the field of view (FOV) of ASCA was within 5° of the Earth's rim. Furthermore for the SIS, we discarded the data acquired when the FOV is within 10° of the bright Earth

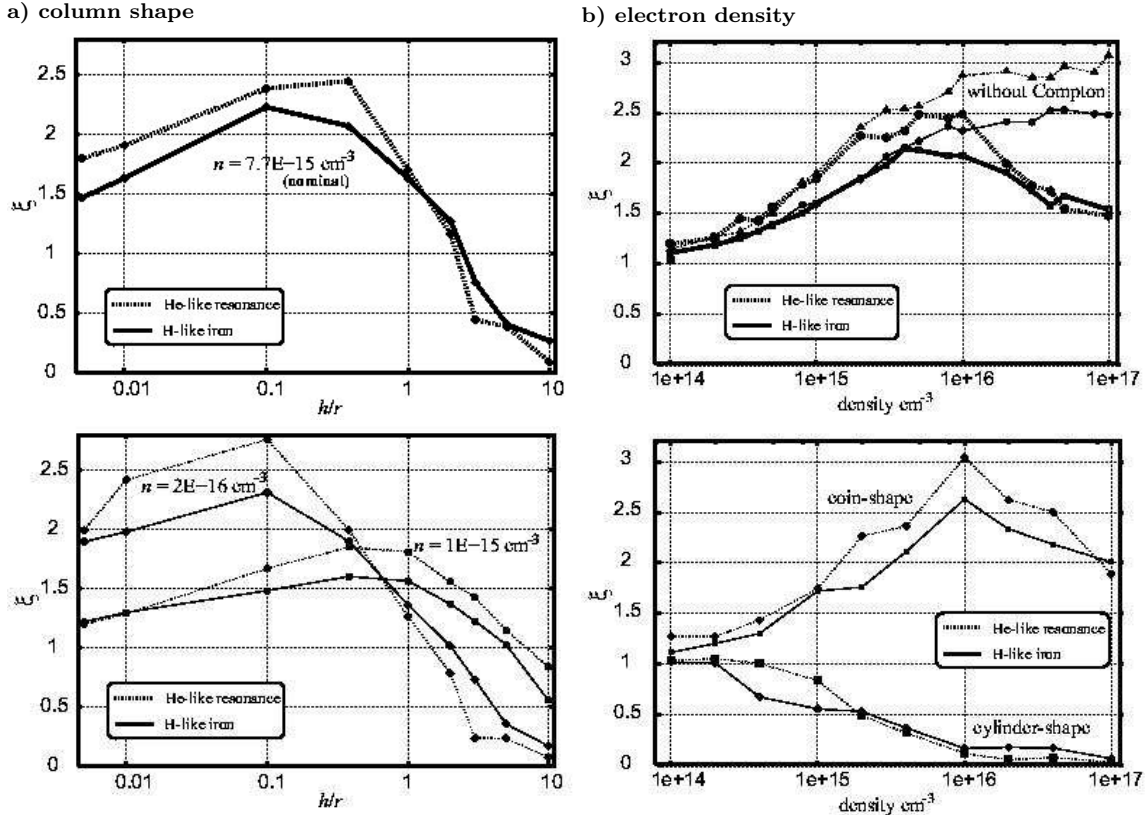


Figure 10. A summary of Monte-Carlo simulations. The beaming factor ξ_m is presented for various column shape and density. The H-like iron line is represented by solid lines and the He-like iron resonance line by dashed lines. The baseline condition of the calculation is given in the text. **a)** The shape dependence of ξ_m , where the volume r^2h is fixed. Calculation is performed for three densities as specified in the figure. **b)** The density dependence of ξ_m for three different column shapes (coin shape, nominal, cylinder shape). The coin shaped column has $r = 1 \times 10^8$ cm and $h = 1 \times 10^7$ cm, while the cylinder shaped column has $r = 1 \times 10^7$ cm and $h = 1 \times 10^8$ cm. The beaming factors without Compton scattering are also shown.

rim and those acquired near the day-night-transition of the spacecraft.

4.2 Light curves

Figure 11 shows the energy resolved light curve of V834 Cen obtained with ASCA SIS+GIS folded by its rotational period, 1.69194 hr (Schwope et al. 1993). The phase is coherent between the two light curves. The pole-on phase of V834 Cen is determined by the optical photometry and polarimetry as shown in table 1 of Bailey et al. (1983), which corresponds to a phase $\phi \sim 0.65\text{--}0.85$ in our X-ray light curve. We can recognize small dips in light curves of the softer two energy bands in figure 11 at $\phi \sim 0.65$ in 1994 and ~ 0.86 in 1999. These dips are thought to arise from photoelectric absorption by the pre-shock matter on the accretion column. Therefore, the pole-on phase is consistent between the optical and X-ray datasets. The folded light curve in the iron line energy band (6.2–7.2 keV) exhibits a hump at or near this pole-on phase, suggesting that the proposed line photon enhancement is indeed taking place in this system. However, detailed examination of the modulation of iron line emission needs phase-resolved spectroscopy, performed in the next subsection.

4.3 spectral analysis

Because the folded light curves (figure 11) have different shapes between the two observations, and because spectral information of GIS-3 in 1994 was degraded by a temporary malfunctioning in the GIS onboard electronics, we use only the 1999 data for spectral analysis. We have accumulated the GIS (GIS2 + GIS3) and SIS (SIS0 + SIS1) data over the pole-on phase ($\phi = 0.73 \pm 0.25$) and side-on phase ($\phi = 0.23 \pm 0.25$) separately. We subtracted the background spectrum, prepared by using the blank sky data of the GIS and SIS. The spectra, thus derived and shown in figure 12, exhibit an absorbed continuum with strong iron K_{α} emission lines over the 6.0–7.2 keV bandpass.

4.3.1 Continuum spectra

We attempted to quantify the 0.8–10.0 keV continua, neglecting for the moment the line energy band of 6.0–7.2 keV. However, the simplest spectral model for polars, namely a single temperature bremsstrahlung continuum absorbed by one single column density, failed to reproduce either of the observed spectra (figure 13 left; Model 1 in table ??). This failure is not surprising, considering that polars generally exhibit multi-temperature hard X-ray emission with complex absorption by the pre-shock absorber (Norton and

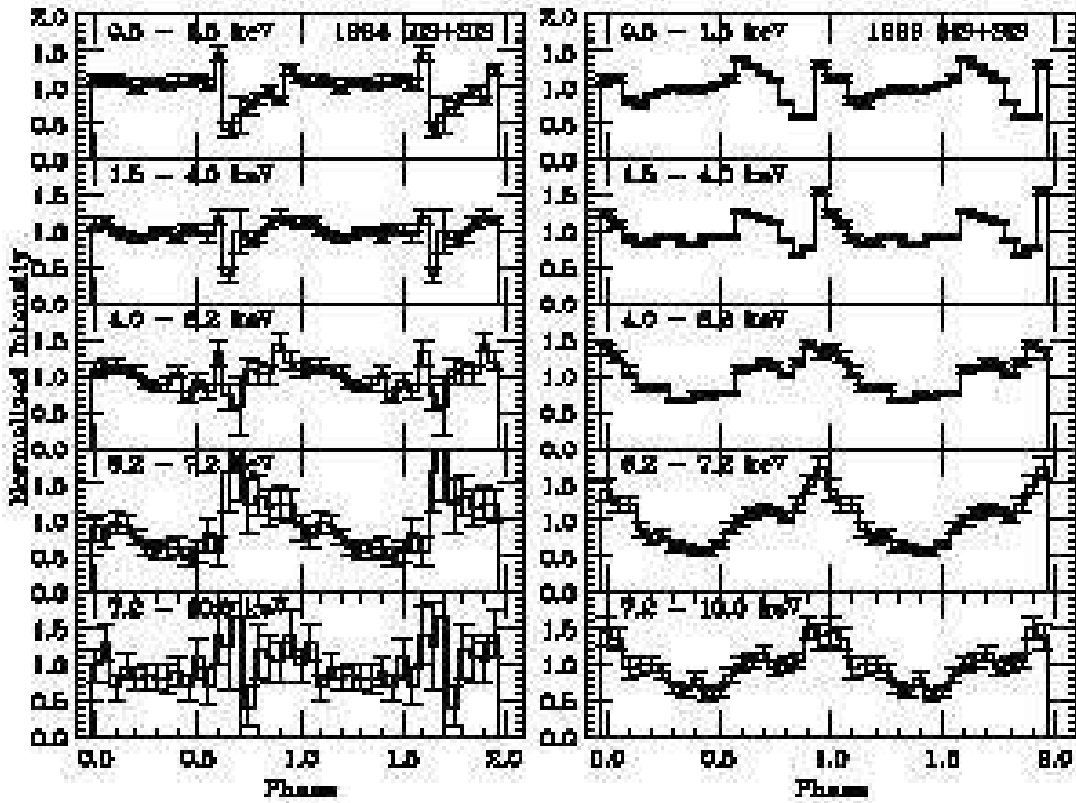


Figure 11. Energy resolved light curves of V834 Cen obtained with ASCA, folded at 1.69194 hr. Phase $\phi = 0$ corresponds to HJD 2445048.9500, which is common to the 1994 and 1999 light curves. Each light curves is shown for two cycles. Left panel shows the observation in 1994, right panel in 1999.

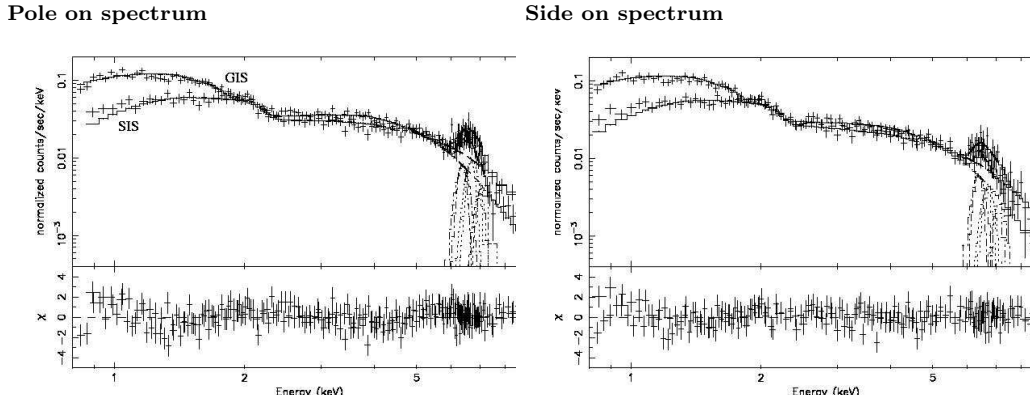


Figure 12. ASCA X-ray spectra of V834 Cen taken in 1999, shown without removing the instrumental responses. Left panel shows the spectra in the pole-on phase ($\phi = 0.73 \pm 0.25$), and right panel those in the side-on phase ($\phi = 0.23 \pm 0.25$). The GIS and SIS data are shown with crosses. The solid crosses show the best-fit model consisting of single temperature bremsstrahlung continuum with partially covered absorption and three narrow Gaussians (see text). The best-fit parameters are shown in table ?? Model 4 and in table 3 (full band fitting). Lower panels show the fit residuals.

Watson 1989). The extremely high temperature obtained by this simple fitting, > 200 keV, is presumably an artifact, compared with the temperature of 14.7 keV measured with Ginga.

To accurately estimate the hottest component of the continuum, avoiding complex absorption in soft energies, we then restricted the fit energy band to a narrower hard en-

ergy band of 4.5 – 10.0 keV (Model 2 in table ??). This lower limit (4.5 keV) was determined in a way described in §3.2 by Ezuka and Ishida (1994). In this case, N_{H} is determined solely by the depth of the iron K-edge absorption at ~ 7.1 keV. This model has been successful on the spectra of both phases, yielding a temperature consistent with the Ginga value. Considering that the K-edge absorp-

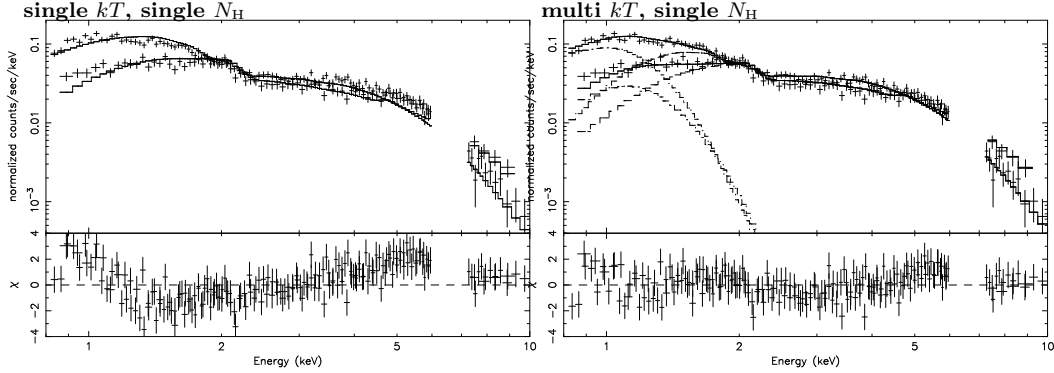


Figure 13. The same spectra as in figure 12 left (pole-on). Left panel shows the best-fit model of single temperature bremsstrahlung absorbed by a single column density. The best-fit parameters are shown in table ?? Model 1. Right panel shows the best-fit model of double temperature bremsstrahlung absorbed by a single column density, corresponding to table ?? Model 3 (free kT).

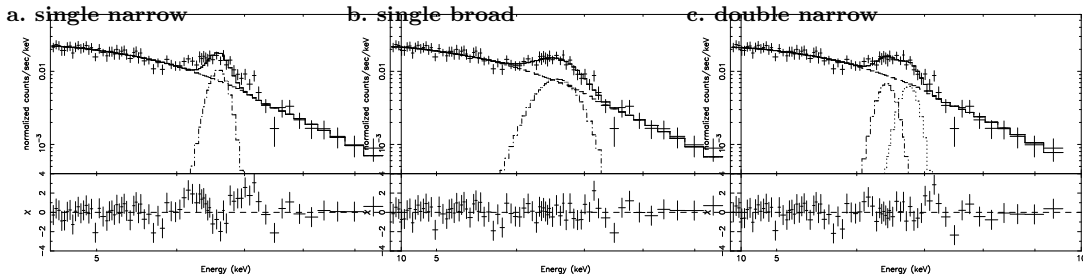


Figure 14. Phase averaged SIS spectra in the iron K-line energy band, fitted with a single narrow Gaussian (left), a single broad Gaussian (center), and a double narrow Gaussian model (right). The continuum spectrum is represented by a single temperature and a single column density in the 4.5 – 10.0 keV band (narrow band fitting). The best-fit parameters are shown in table 2.

tion in the observed spectra are relatively shallow, the value of N_{H} obtained in this way is thought to approximate the covering-fraction-weighted mean value of multi-valued absorption. The mean value of N_{H} in the accretion column is hence inferred to be $\sim 10^{23} \text{ cm}^{-2}$.

We next fitted the original 0.8 – 10.0 keV spectra (but excluding the iron K line region) by a two-temperature bremsstrahlung with single N_{H} , and obtained acceptable results (right panel of figure 13 and Model 3 in table ??). However, the first temperature kT_1 is still poorly determined; the fit became unacceptable for the pole-on spectra when we fixed kT_1 to the Ginga value. Furthermore, the obtained N_{H} is about $1 \times 10^{22} \text{ cm}^{-2}$ in either case, which is not consistent with the inference from the narrow band fitting. Thus, we regard Model 3 as inappropriate.

A fourth spectral model we employed consists of a single temperature bremsstrahlung and double-valued photoelectric absorption ($N_{\text{H}1}$ and $N_{\text{H}2}$), which is so-called partial covered absorption model (PCA model). This model has been fully acceptable for both phases (Model 4 in table ??). The obtained $N_{\text{H}2}$ is consistent with that suggested by the narrow band fitting, and the fit remained good even when we fix the temperature to the Ginga value. We therefore utilize this model (Model 4) as the best representation of the continua for both phases. The solid curves in figure 12 refer to this modeling.

4.3.2 The Fe-K lines

Having quantified the continuum spectra of V834 Cen, we proceed to the study of the iron K-line. For this purpose, we employ the phase-averaged spectrum, and again limit the energy range to the 4.5 – 10.0 keV band to avoid complex absorption structure in lower energies. As a first-cut attempt, we modeled the iron line with a single Gaussian model, while represented the continuum with a single-temperature bremsstrahlung absorbed with a single column density (to reproduce the iron K edge), but the fit failed to reproduce the line profile as shown in figure 14a. A broad Gaussian model with $\sigma \sim 0.28 \text{ keV}$ has been found to be successful (table 2; figure 14b), but the obtained line centroid energy is too low for ionized Fe-K species that are expected for a plasma of temperature $\sim 10 \text{ keV}$. We can alternatively fit the data successfully with two narrow Gaussians (table 2; figure 14c), where the centroid energy of the first Gaussian turned out to be consistent with that of the fluorescent iron K_{α} line (6.40 keV); that of the second Gaussian comes in between those of He-like iron K_{α} line (6.65 – 6.70 keV) and H-like line (6.97 keV). This means that the second Gaussian is in reality a composite of the H-like and He-like lines.

We therefore employed a line model consisting of three narrow Gaussian, each having a free centroid energy and a free normalization. We have then obtained an acceptable fit, with the three centroid energies consistent with the Fe-K line energies of the neutral, He-like, and hydrogen-like species, as shown in figure 15. These three lines have been observed in

Table 1. Best Fit continuum parameters for the GIS and SIS spectra of V834 Cen^a.

Model ^b	kT_1 keV	kT_2 keV	$N_{\text{H}1}$ $\times 10^{22} \text{ cm}^{-2}$	$N_{\text{H}2}$ $\times 10^{22} \text{ cm}^{-2}$	Cov. Frac ^c %	χ^2_{ν} (dof)
POLE-ON phase						
Model 1	> 200	–	$0.12^{+0.02}_{-0.02}$	–	–	2.19 (188)
Model 2 ^d	$10.8^{+26.8}_{-4.8}$	–	$14.5^{+8.1}_{-8.0}$	–	–	0.49 (94)
Model 3	> 158	$0.19^{+0.01}_{-0.01}$	$0.82^{+0.08}_{-0.08}$	–	–	1.01 (186)
	14.7 ^e	$0.15^{+0.01}_{-0.01}$	$1.21^{+0.08}_{-0.08}$	–	–	1.64 (187)
Model 4	> 164	–	< 0.02	$7.41^{+2.26}_{-1.70}$	$41.3^{+3.4}_{-3.3}$	0.91 (186)
	14.7 ^e	–	< 0.08	$8.83^{+1.90}_{-1.59}$	$60.4^{+2.4}_{-2.5}$	1.00 (187)
SIDE-ON phase						
Model 1	> 171	–	< 0.04	–	–	1.00 (174)
Model 2 ^d	$12.4^{+180}_{-7.1}$	–	$13.9^{+11.3}_{-11.2}$	–	–	0.47 (70)
Model 3	> 200	$0.25^{+0.03}_{-0.03}$	$0.36^{+0.12}_{-0.13}$	–	–	0.85 (172)
	14.7 ^e	$0.18^{+0.01}_{-0.01}$	$0.78^{+0.10}_{-0.10}$	–	–	1.135 (173)
Model 4	> 49.3	–	< 0.02	$12.7^{+12.5}_{-1.2}$	$35.6^{+10.0}_{-14.1}$	0.81 (172)
	14.7 ^e	–	< 0.06	$11.2^{+4.5}_{-3.4}$	$50.7^{+5.4}_{-5.1}$	0.85 (173)
Phase average						
Model 2 ^d	$11.7^{+15.2}_{-4.4}$	–	$14.0^{+5.8}_{-4.2}$	–	–	0.49 (122)
Model 4	14.7 ^e	–	< 0.06	$9.79^{+1.69}_{-1.47}$	$56.9^{+2.1}_{-2.1}$	1.07 (275)

^a Excluding the Fe K_{α} line band (6.0 – 7.2 keV).

^b Model 1/2: single N_{H} , single kT . Model 3 : single N_{H} , multi kT .

Model 4: multi N_{H} , single kT .

^c The covering fraction (%) of $N_{\text{H}1}$.

^d Fitting in the 4.5 – 10.0 keV band. For other models, the 0.8 – 10.0 keV band is used.

^e Continuum temperature fixed at the value measured with Ginga (Ishida et al. 1991).

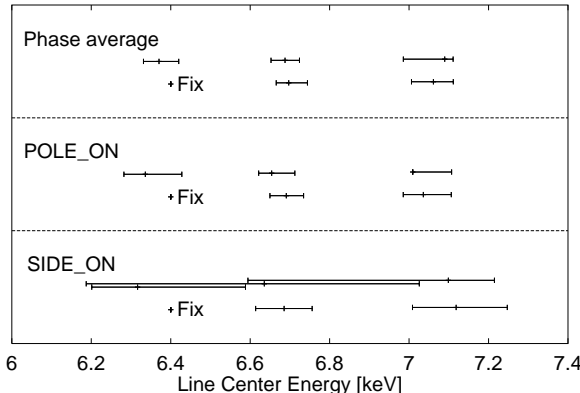


Figure 15. The best-fit line centroid energies with 68 % errors in terms of the three narrow Gaussian model. From the top to bottom panels, the results for the phase average, pole-on phase, and side-on phase are shown. The upper plot in each panel shows the results when three centroid energies are left free. The lower plot shows the results when the centroid energy of the first Gaussian is fixed at 6.40 keV. The fit energy range is 4.5 – 10.0 keV.

the spectra of many polars with ASCA (Ezuka and Ishida 1999). Hereafter, we adopt the three narrow Gaussian model in quantifying the iron lines of V834 Cen.

As our final analysis, we have repeated the three-Gaussian fitting to the spectra, by fixing the line centroid energy of the first Gaussian (identified to a fluorescent line) at 6.40 keV. The result is of course successful, and the obtained parameters are given in table 3 as well as figure 15. Figure 16 shows the phase-resolved SIS spectra fitted with

this model. For consistency check, we have expanded the fit energy range back to 0.7 – 10.0 keV, and performed full-band fitting, employing the continuum Model 4 and the three narrow Gaussian for the iron K-line. The results, presented in table 3, are generally consistent with those from the narrow-band analysis.

The temperature and N_{H} obtained in these final fits are thus the same between the two phases within errors, and the EW of fluorescent and H-like lines are also consistent with being unmodulated. In contrast, the EW of the He-like line is enhanced by $(\xi_{\text{pole}}/\xi_{\text{side}})^{\text{obs}} \equiv 1.87^{+0.54}_{-0.54}$ times (narrow band fitting) or $1.91^{+0.47}_{-0.64}$ times (full band fitting) in the pole-on phase compared to the side-on phase, with > 90 % statistically significance.

5 DISCUSSION

5.1 Origin of the line intensity modulation in V834 Cen

In order to verify our interpretation, mentioned in section 2, we observed the polar V834 Cen with ASCA. The EW of the He-like iron- K_{α} line has been confirmed to be enhanced by a factor of $(\xi_{\text{pole}}/\xi_{\text{side}})^{\text{obs}} = 1.87 \pm 0.54$ in the pole-on phase relative to the side-on phase. Can we explain the observed rotational modulation of the He-like iron line EW of V834 Cen by some conventional mechanisms? An obvious possibility is that the temperature variation modulates the iron line intensity. However, the continuum temperature determined by the narrow band fitting (table 3) is almost constant within the error to explain the rotational modulation of the line intensity ratio. Alternatively, the bottom

Table 2. Best Fit parameters of the iron K_{α} line^a.

Line model	iron K_{α} line				statistics
	L.C. 1 ^b (keV)	σ_1 (keV)	L.C. 2 ^b (keV)	σ_2 (keV)	
single narrow	$6.63^{+0.04}_{-0.05}$	0.0001^c	—	—	χ^2_{ν} (dof) 1.37 (69)
single broad	$6.66^{+0.05}_{-0.05}$	$0.29^{+0.06}_{-0.05}$	—	—	0.66 (68)
double narrow	$6.45^{+0.08}_{-0.11}$	0.0001^c	$6.79^{+0.23}_{-0.46}$	0.0001^c	0.91 (67)

^a The phase averaged spectrum. Only SIS data are used for the fitting.
Fitted with a single temperature and single column density model in 4.5–10.0 keV.
Fixed the continuum temperature and N_{H} to the Model2 in table ??

^b Line center energies.

^c Fixed.

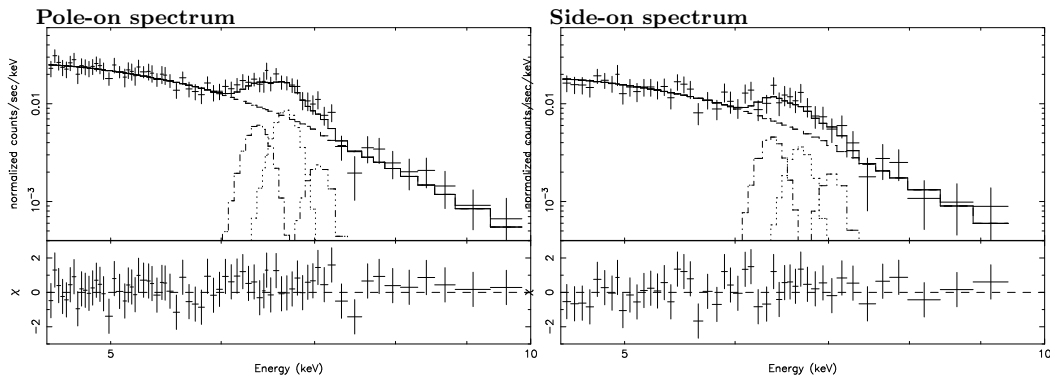


Figure 16. Phase resolved spectra over the Fe-K line energies, fitted with three narrow Gaussians. The central energy of the first Gaussian is fixed at 6.4 keV. The best-fit parameters are shown in table 3.

part of the accretion column, where the emissivity of the He-like iron line is highest (figure 5), may be eclipsed by the WD surface so that the He-like line is reduced in the side-on phase. However, such a condition does not occur under the geometrical parameters of V834 Cen. Furthermore, we do not see any dip in the rotation-folded hard X-ray light curve. Therefore, this explanation is not likely, either. A third possibility is that a part of iron line photons come from some regions other than the accretion column. In fact, X-rays from polars are known to be contributed by photons reflected from the WD surface (Beardmore et al. 1995; Done & Beardmore 1995; Done & Magdziarz 1998). This mechanism can explain the production of fluorescent lines, and possibly its rotational modulation, but cannot produce highly ionized iron lines. From these considerations, we conclude that the observed iron line modulation is difficult to account for without appealing to the resonance scattering effects.

Our next task is to examine whether the geometrical collimation mechanism (§ 2.1) can explain the observation. When the optical depth of resonance scattering is very high and hence the line photons come solely from the surface of the accretion column, the angular distribution of the iron line intensity is given analytically by equation (B1) in Appendix B. By averaging this distribution under the geometry of V834 Cen, and taking into account the exposure for the two phases, we have calculated the expected line beaming factor ξ for the ASCA data as shown in Figure 17. Thus,

to explain the observed enhancement of He-like line solely by the geometrical beaming, a very flat coin-shaped column with $h/r \sim 0.2$ would be required. Furthermore, the observed ξ should be lower by about 30–40% than the ideal calculation in Figure 17, because finite optical depths, expected under a typical plasma density of polar accretion column, reduce the enhancement (Figure 7). We hence conclude that the geometrical mechanism alone is insufficient to explain the observed He-like iron line enhancement in V834 Cen (§ 2), and hence the additional collimation due to the velocity gradient effect is needed.

Then, are all the observed results consistently explained in our picture that incorporates the geometrical and velocity-gradient effects? At the temperature of V834 Cen (~ 15 keV), the resonant photons in fact contribute about 65% to the observed He-like iron K_{α} line, the rest coming from intercombination ($\sim 20\%$) and forbidden ($\sim 15\%$) lines which are free from the resonance scattering effects (figure 4). As a result, the line collimation is expected to be somewhat weakened in the ASCA spectra, where we cannot separate these unmodulated lines from the resonance line. After correcting for this reduction, the true value of ξ for the He-like resonance line is calculated to be ~ 2.3 . This is within the range that can be explained by our scenario.

How about the H-like iron K_{α} line? Even though it consists entirely of resonant photons, its modulation in the V834 Cen data has been insignificant (table 3). Presumably, this is mainly due to technical difficulties in detecting this weak

Table 3. Best Fit parameters of the iron K_{α} line with three narrow gaussians.

Phase ^a	continuum		Fluorescent		He-like		H-like		χ^2_{ν} (dof)
	kT (keV)	N_{H} $\times 10^{22} \text{ cm}^{-2}$	EW (eV)	l. c. ^b (keV)	EW (eV)	l. c. ^b (keV)	EW (eV)		
Narrow Band Fitting^c									
Average	$9.3^{+10.4}_{-2.9}$	$15.4^{+5.9}_{-5.8}$	244^{+59}_{-83}	$6.70^{+0.06}_{-0.04}$	352^{+90}_{-91}	$7.07^{+0.08}_{-0.04}$	192^{+81}_{-97}	0.67 (154)	
Pole-on	$9.6^{+20.3}_{-2.87}$	$15.6^{+8.0}_{-6.5}$	242^{+87}_{-102}	$6.69^{+0.07}_{-0.05}$	417^{+104}_{-113}	$7.04^{+0.14}_{-0.15}$	223^{+123}_{-118}	0.59 (140)	
Side-on	$9.0^{+50.0}_{-1.0}$	$16.6^{+13.4}_{-9.5}$	270^{+122}_{-175}	$6.69^{+0.70}_{-0.13}$	223^{+94}_{-101}	$7.14^{+0.16}_{-0.48}$	223^{+123}_{-89}	0.64 (103)	
Full Band Fitting^d									
Average			347^{+53}_{-52}	$6.71^{+0.05}_{-0.06}$	456^{+57}_{-70}	$7.07^{+0.10}_{-0.08}$	230^{+88}_{-56}	1.05 (327)	
Pole-on	(Model 4 in table ??) ^e		229^{+164}_{-17}	$6.71^{+0.07}_{-0.10}$	650^{+19}_{-164}	$7.06^{+0.12}_{-0.15}$	282^{+58}_{-164}	0.98 (243)	
Side-on			368^{+76}_{-119}	$6.71^{+0.62}_{-0.13}$	341^{+115}_{-111}	$7.13^{+0.21}_{-0.56}$	222^{+199}_{-105}	0.82 (210)	

^a Pole-on phase: $\phi = 0.73 \pm 0.25$. Side-on phase: $\phi = 0.23 \pm 0.25$.

^b The line center (keV). That of the fluorescent component is fixed at 6.40 keV.

^c The determination of continuum spectrum is performed in 4.5 keV – 10.0 keV with a single N_{H} and single temperature model.

^d The determination of continuum spectrum is performed in 0.8 keV – 10.0 keV with a multi N_{H} and single temperature model (Model 4 in table ??).

^e The temperature is fixed to the Ginga value. Continuum parameters are fixed.

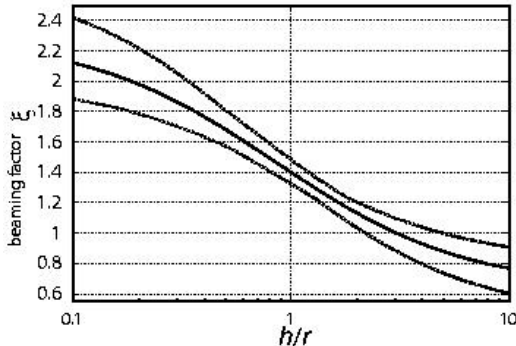


Figure 17. The expected line beaming factor $\xi_{\text{pole}}/\xi_{\text{side}}$ of V834 Cen due to pure geometrical effects at the limit of large optical depth, calculated by considering the system geometry of V834 Cen and the exposure for each phase. It is shown as a function of h/r . The solid line corresponds to the most likely system geometry of $(i, \beta) = (45^\circ, 25^\circ)$, while dashed lines reflect uncertainties in the system geometry.

line, under the presence of the stronger He-like line adjacent to it. Furthermore, we expect the hydrogen-like iron line to be intrinsically less collimated than the He-like resonance iron line, because the H-like line photons are produced predominantly in the top regions of the accretion column (figure 5): there, the electron density is lower, thermal Doppler effect is stronger, and the path of escape from the column is shorter, as compared to the bottom region where the He-like lines are mostly produced. Therefore, the H-like line is expected to be less collimated than the He-like resonance line (figure 18). Note in the observation blended He-like line is almost the same collimation as H-like line.

From these considerations, we conclude that the ASCA results on V834 Cen can be interpreted consistently by our POLE scenario.

5.2 Determination of the accretion column parameters

The line beaming effect we have discovered is expected to provide unique diagnostics of the accretion column of magnetic WDs. The physical condition in the accretion column is described by four parameters: kT^{sh} , h , r , and n_e^{sh} . To determine these parameters, four observational or theoretical constraints are required. Usually, observations provide two independent quantities, the temperature kT_{OBS} and the volume emission measure VEM, which is $\sim (n_e^{\text{sh}})^2 \cdot hr^2$. Also there is one theoretical constraint, that the shock heated plasma cools only by the free-free cooling, which relates kT^{sh} , n_e^{sh} , and h as in equation (A5).

With these three constraints, and taking into account the Aizu's solution (1973), we can express h and r as

$$h = 1.61 \times 10^7 \text{ cm} \left(\frac{kT^{\text{sh}}}{17.7 \text{ keV}} \right)^{\frac{1}{2}} \left(\frac{n_e^{\text{sh}}}{10^{16} \text{ cm}^{-3}} \right)^{-1} \quad (12)$$

$$r = 2.15 \times 10^7 \text{ cm} \left(\frac{\text{VEM}}{1.30 \times 10^{54} \text{ cm}^{-3}} \right) \left(\frac{kT^{\text{sh}}}{17.7 \text{ keV}} \right)^{-\frac{1}{4}} \times \left(\frac{n_e^{\text{sh}}}{10^{16} \text{ cm}^{-3}} \right)^{-\frac{1}{2}}. \quad (13)$$

Here, we normalized the VEM to the value of $1.30 \times 10^{54} \text{ cm}^{-3}$ obtained from V834 Cen, adopting a distance of 86 pc (Warner 1987). The value of $kT^{\text{sh}} = 17.7 \text{ keV}$ was determined from the expected mass of WD by the observed ratio of H-like to He-like iron K_{α} lines, considering the vertical temperature gradient (Ezuka and Ishida 1999 figure 5); it is consistent with an independent calculation by Wu et al (1995) based on the Ginga observation (Ishida 1991). When n_e^{sh} is low, the solutions to h and r imply a long cylinder-like column, while a flat coin-shaped geometry is indicated by high values of n_e^{sh} . However, due to the lack of one more piece of information, the value of n_e^{sh} has so far been left undetermined. As a consequence, we have not been able to determine the column geometry.

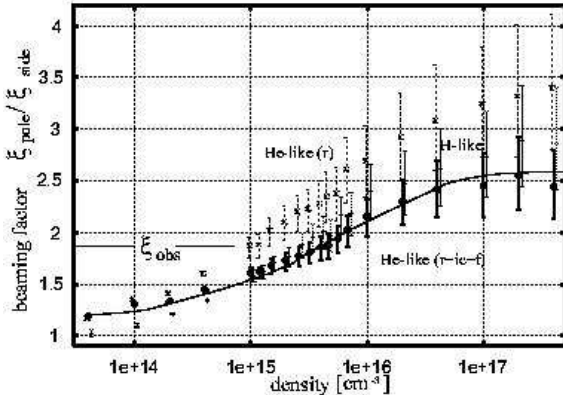


Figure 18. The expected beaming factor $\xi_{\text{pole}}/\xi_{\text{side}}$ of V834 Cen, calculated by Monte-Carlo simulations under the actual observing condition with ASCA, and shown as a function of the assumed post-shock density. The shock temperature is set to 17.7 keV, and the volume emission measure is set to $1.30 \times 10^{54} \text{ cm}^{-3}$. The dashed and dotted data points indicate ξ of He-like and H-like resonance iron K_{α} photons, respectively. The solid data points show ξ of the blended He-like iron line, which includes intercombination and forbidden lines. The error bars take into account those of the geometrical parameters.

The present work provides us with the needed fourth information, the value of ξ , which reflects the accretion column condition. Suppose we specify a value of n_e^{sh} . Then, equations (12) and (13) determine h and r respectively, which in turn are used as inputs to the Monte-Carlo simulation to predict ξ . In this way, we have calculated ξ for V834 Cen as a function of n_e^{sh} , and show the results in Figure 18. By comparing it with the observed value of $(\xi_{\text{pole}}/\xi_{\text{side}})^{\text{obs}} \sim 1.87$, we obtain the best estimate as $n_e^{\text{sh}} \sim 4.6 \times 10^{15} \text{ cm}^{-3}$. This in turn fixes the column height as $h \sim 3.5 \times 10^7 \text{ cm}$ and the radius as $r \sim 3.2 \times 10^7 \text{ cm}$. These values are considered typical for polars.

Currently, the errors on $\xi_{\text{pole}}/\xi_{\text{side}}$ are so large that the value of n_e^{sh} is uncertain almost by an order of magnitude, with the allowed range being $1 \times 10^{14} - 1 \times 10^{16} \text{ cm}^{-3}$. However, our new method will provide a powerful tool for next generation instruments with a larger effective area and an improved energy resolution.

5.3 Effects on the abundance estimates

The iron abundance of other polars, measured by Ezuka & Ishida (1999), are subject to some changes when we properly consider the resonance scattering effects. For this purpose, we show in table 4 the geometrical parameters (i and β) of 17 polars, which have been randomly selected from currently-known ~ 50 polars. The expected enhancement $\zeta \equiv \sum_{\text{phase}} \xi$ are also listed with assumption that the resonance lines are collimated as much as that in the case of V834 Cen. Thus, the implied corrections to the iron abundances of these objects are at most $\pm 30\%$, which is generally within the measurement error. Polars with almost side-on or almost pole-on geometry, like POLEs, are subject to a relatively large modification in the abundance estimates, but such a geometry is a rare case (here, only VY For). Therefore, the distribution

of metal abundances of polars, 0.1 – 0.8 solar, measured by Ezuka & Ishida (1999) is considered still valid.

5.4 Mystery of POLEs

Our Monte-Carlo simulation (§3) and the observed study of V834 Cen (§4) consistently indicate that the resonance iron K lines are enhanced by a factor of $\xi_m = 2 - 2.5$ in the axial direction of accretion column. The effect is thought to be ubiquitous among polars, because we have so far employed very typical conditions among them. Consequently, if a polar with co-aligned magnetic axis ($\beta \sim 0$) is viewed from rear the pole-on direction ($i \sim 0$), we expect the iron K line EW to be persistently enhanced by 2 - 2.5 times. When this enhancement is not considered, such objects would yield artificially higher metallicity by similar factors. We conclude that the three POLEs (§1) are exactly such objects.

In condition of $\zeta > 2$, the extremely high face-value abundances of AX J2315-0592 will be modified to be ~ 1 solar, and abundance of RX J1802.1+1804 or AX J1842-0423 comes into the measured distribution of other polars within error. We can expect a strong collimation with an adequate density of $n_e \sim 10^{16} \text{ cm}^{-3}$ (figure 10b) and an adequate shape of $h/r \sim 0.1-0.5$ (figure 10a) with typical radius $\sim 10^7 \text{ cm}$. Thus, one example of strong collimation calculated for He-like iron resonance line is in the condition that temperature of 10 keV, $r = 5 \times 10^7 \text{ cm}$, $n_e = 7.9 \times 10^{15} \text{ cm}^{-3}$ and VEM = 10^{55} cm^{-3} , which yield an X-ray luminosity of $1.0 \times 10^{32} \text{ erg s}^{-1}$ (2 – 10 keV). Hereafter, we call this condition the strong case. Figure 19 shows the expected enhancement ζ of iron He-like line (sum of resonance line, intercombination line and forbidden line) with various geometrical conditions (i and β). In figure 20, we have converted the result of figure 19 into cumulative probability distribution of ζ . We hence expect $\zeta > 2$ at the condition of strong case shown above, with a probability of $\sim 4.5\%$. This estimate is in an rough agreement with the observation, i.e. the three POLEs among the known ~ 50 polars. We reconfirms that the iron abundances derived from the observation (Ezuka & Ishida 1999) remains valid to within 30 % for a major fraction of polars. Thus, we conclude that the mystery of POLEs have been solved by the proposed line-collimation mechanism.

6 CONCLUSION

In order to explain the extremely intense iron K lines observed from several Galactic X-ray sources (including two polars; section 1), we have developed a scenario of POLEs, that the iron lines from accretion poles of magnetic WDs are axially collimated by the two mechanisms (section 2) which become operational under large optical depths for the resonant line scattering. One is the geometrical effect which becomes effective when the accretion column is rather short, while the other is a physical mechanism that the Doppler shifts due to vertical velocity gradient in the post-shock flow reduces the cross section for resonance scattering along the field lines.

In section 3, we have carried out Monte-Carlo simulations, and confirmed that the velocity-gradient effect, augmented by the geometrical effect, can enhance the iron K

Table 4. Geometrical parameters of randomly sampled polars, and values of ζ expected for them

object name	i^a	β^b	ζ^c	reference
BL Hyi	70 ± 10	153 ± 10	0.70	Cropper 1990
UZ For	~ 88	~ 14	0.71	Ferrario et al. 1989
VV Pup	76 ± 6	152 ± 6	0.71	Cropper 1990
ST LMi	64 ± 5	141 ± 4	0.71	Cropper 1990
AN UMa	65 ± 20	20 ± 5	0.87	Cropper 1990
QQ Vul	65 ± 7	~ 23	0.88	Cropper 1990, Schwope et al. 2000, Catalan et al. 1999
V1309 Ori	~ 80	~ 30	0.86	Harrop-Allin et al. 1997
EF Eri	58 ± 12	27 ± 18	0.96	Cropper 1990
AR UMa	50 ± 10	23 ± 13	1.05	Szkody et al. 1999
WW Hor	~ 74	~ 48	1.06	Bailey et al. 1988
DP Leo	76 ± 10	103 ± 5	1.06	Cropper 1990
MR Ser	43 ± 5	38 ± 5	1.09	Cropper 1990
J1015+0904	55 ± 5	43 ± 7	1.10	Burwitz et al. 1998
V834 Cen	45 ± 9	25 ± 5	1.11	Cropper 1990
AM Her	52 ± 5	66 ± 5	1.13	Wickramasinghe et al. 1991, Ishida et al. 1997
EK UMa	56 ± 19	56 ± 19	1.14	Cropper 1990
VY For	9 ± 3	~ 9	1.66	Beuermann et al. 1989

a Inclination angle (degrees).

b Pole colatitude (degrees).

c Expected beaming factor to the average flux, assuming that the same collimation as the case of V834 Cen occurs and that only single accretion column emits.

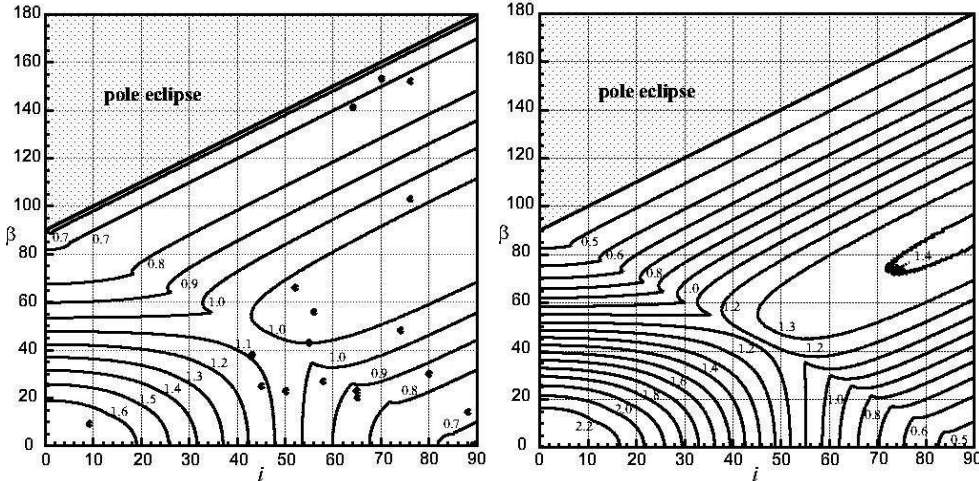


Figure 19. The expected enhancement ζ to the average line intensity calculated on the plane of (i, β) , assuming that accretion column exists only on one pole with the same collimation as the case of V834 Cen (left) or the strong case shown in text (right). Contour levels are shown in the figure. The polars listed in table 4 are also plotted in the left panel with tick marks.

line EW in the pole-on direction up to a factor of 3.0 as compared to the angular average. This is higher than the maximum collimation available with the geometrical effect alone (Appendix B).

In order to experimentally verify our interpretation, we have analyzed in section 4 the ASCA data of V834 Cen, which has a suitable geometry in that our line-of-sight to the accretion column changes from 20° to 70° as the WD rotates. Through detailed phase-resolved X-ray spectroscopy, the EW of the He-like iron- K_α line has been confirmed to be enhanced by a factor of $(\xi_{\text{pole}}/\xi_{\text{side}})^{\text{obs}} = 1.87 \pm 0.54$. In section 5.1, we have examined whether the observation can be explained away by any other mechanism, and we have con-

cluded that this observational result of V834 Cen strongly reinforces our interpretation of POLEs.

Although the resonance lines are collimated with the proposed beaming effect, the previous measurements of the distribution of metal abundances of polars is considered still valid (section 5.3) except for POLEs. With proposed mechanism, the extremely high face-value abundances observed in POLEs can be reconciled with the average abundance measured from the other polars. Thus, the POLE scenario successfully solves the mystery of the extremely strong iron lines observed from the three X-ray sources.

In addition, our scenario provides a new method of unique determination of physical condition in the accretion

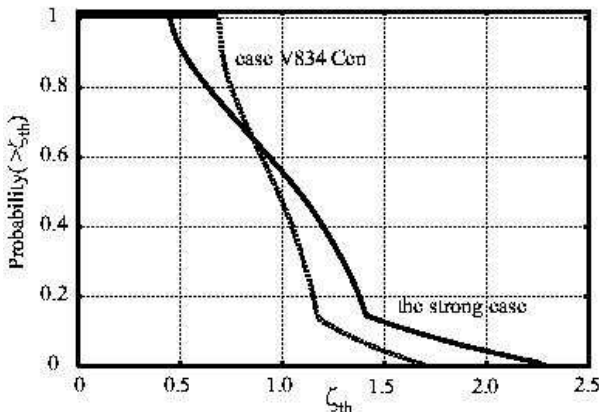


Figure 20. The cumulative probability distribution of finding ζ higher than the specified threshold ζ_{th} , assuming that objects are randomly distributed in terms of i and β . The dotted and solid curves represent the case of V834 Cen and the strong case, respectively.

column, using the beaming factor of resonance lines as a new observational information (section 5.2). This will be a powerful method for the next generation instruments.

We thank the members of the ASCA team for spacecraft operation and data acquisition.

APPENDIX A: PLASMA IN AN ACCRETION COLUMN OF A WD

A flow of accreting matter captured by the magnetic field of WD channels into an accretion column, where a standing shock forms and heats up the matter to a temperature kT^{sh} of

$$\begin{aligned} kT^{\text{sh}} &= \frac{3}{8} \frac{GM_{\text{WD}}\mu m_{\text{H}}}{R_{\text{WD}}} \\ &= 16 \left(\frac{\mu}{0.615} \right) \left(\frac{M_{\text{WD}}}{0.5M_{\odot}} \right) \left(\frac{R_{\text{WD}}}{10^9 \text{cm}} \right)^{-1} \text{keV}, \end{aligned} \quad (\text{A1})$$

where k is the Boltzmann constant, G is the gravitational constant, M_{WD} is the WD mass (typically $0.5M_{\odot}$), and R_{WD} is the radius of the WD (typically 10^9 cm). So the plasma has a typical temperature of hard X-ray emitter, forming an accretion column illustrated in figure 1. The velocity beneath the shock front u^{sh} is described with relation to the free-fall velocity u_{ff} as

$$\begin{aligned} u^{\text{sh}} &= \frac{u_{\text{ff}}}{4} = \frac{1}{4} \sqrt{\frac{2GM_{\text{WD}}}{R_{\text{WD}}}} \\ &= 0.9 \times 10^8 \left(\frac{M_{\text{WD}}}{0.5M_{\odot}} \right)^{1/2} \left(\frac{R_{\text{WD}}}{10^9 \text{cm}} \right)^{-1/2} \text{cm/s}. \end{aligned} \quad (\text{A2})$$

Assuming that the plasma is a single fluid and that the abundance is one solar, the electron density of the post-shock plasma is given as

$$\begin{aligned} n_e^{\text{sh}} &\simeq \left(\frac{\dot{M}}{\pi r^2 u^{\text{sh}} \mu m_{\text{H}}} \right) \times 0.518 \\ &= 7.7 \times 10^{15} \left(\frac{\dot{M}}{10^{16} \text{g s}^{-1}} \right) \left(\frac{M_{\text{WD}}}{0.5M_{\odot}} \right)^{-1/2} \left(\frac{R_{\text{WD}}}{10^9 \text{cm}} \right)^{1/2} \end{aligned}$$

$$\times \left(\frac{r}{5 \times 10^7 \text{cm}} \right)^{-2} \text{cm}^{-3}, \quad (\text{A3})$$

where the value 0.518 is the fraction of electron density to the total density assuming the solar abundances. In the accretion column, kT , u and n_e all have a vertical gradient from the shock front toward the WD surface. Numerically, the vertical profiles of these quantities as a function of the distance z from the WD surface, normalized by h , are calculated by Aizu (1973) as

$$\frac{kT}{kT^{\text{sh}}} = \frac{v}{u^{\text{sh}}} = \left(\frac{n_e}{n_e^{\text{sh}}} \right)^{-1} \simeq \left(\frac{z}{h} \right)^{\frac{2}{5}}, \quad (\text{A4})$$

where each quantity is normalized to its value immediately below the shock front; kT^{sh} , u^{sh} , and n_e^{sh} .

The column radius of the accretion column is typically $r = 5 \times 10^7$ cm. Since the shock front is sustained by the pressure of the post-shock plasma against the gravity, h is described by free-free cooling time scale $t_{\text{ff-cool}}$ of the heated plasma as $h \sim u^{\text{sh}} t_{\text{ff-cool}}$. According to Aizu (1973), h is given more specifically as

$$\begin{aligned} h &= 0.605 u^{\text{sh}} t_{\text{ff-cool}} \\ &= 1.9 \times 10^7 \left(\frac{kT^{\text{sh}}}{16 \text{keV}} \right)^{\frac{1}{2}} \left(\frac{n_e^{\text{sh}}}{7.7 \times 10^{15} \text{cm}^{-3}} \right)^{-1} \text{cm} \end{aligned} \quad (\text{A5})$$

where $t_{\text{ff-cool}}$ is given by

$$\begin{aligned} t_{\text{ff-cool}} &\equiv \frac{3n_e kT^{\text{sh}}}{2\epsilon_{\text{ff}}} \\ &= 0.35 \left(\frac{kT^{\text{sh}}}{16 \text{keV}} \right)^{\frac{1}{2}} \left(\frac{n_e^{\text{sh}}}{7.7 \times 10^{15} \text{cm}^{-3}} \right)^{-1} \text{s} \end{aligned} \quad (\text{A6})$$

with ϵ_{ff} being the volume emissivity of free-free emission [eq. (5.15) in Rybicki & Lightman 1979]. Note that the ion to electron energy transfer time scale t_{eq}

$$t_{\text{eq}} = 5.6 \times 10^{-3} \left(\frac{kT^{\text{sh}}}{16 \text{keV}} \right)^{\frac{3}{2}} \left(\frac{n_e^{\text{sh}}}{7.7 \times 10^{15} \text{cm}^{-3}} \right)^{-1} \quad (\text{A7})$$

[see eq (5.31) in Spitzer 1962] is much shorter than $t_{\text{ff-cool}}$, so the ions and electrons are thought to share the same temperature.

At the temperature of a few tens keV [equation (A1)], the electron scattering dominates the opacity in the hard X-ray band. Actually, the optical depth of the accretion column for free-free absorption, τ_{ff} , is given, relative to the electron scattering optical depth τ_{T} [equation (1)] as

$$\begin{aligned} \tau_{\text{ff}} &= 0.88 \times 10^{-10} \tau_{\text{T}} \left(\frac{E}{6 \text{keV}} \right)^{-2} \left(\frac{kT}{16 \text{keV}} \right)^{-\frac{3}{2}} \\ &\times \left(\frac{n_e^{\text{sh}}}{7.7 \times 10^{15} \text{cm}^{-3}} \right) \end{aligned} \quad (\text{A8})$$

[see equation (5.18) in Rybicki & Lightman 1979]. Thus, the free-free absorption is negligible compared to Thomson scattering.

The cross section of resonance scattering σ_{RS} for a photon with energy E_0 can be described generally as

$$\sigma_{\text{RS}} = \frac{\pi e^2}{m_i c} f_{12} \frac{1}{\sqrt{2\pi\Delta E}} \exp \left\{ -\frac{(E_0 - E_{\text{RS}})^2}{2\Delta E^2} \right\} \text{cm}^{-3} \quad (\text{A9})$$

where f_{12} is the oscillator strength for Lyman- α transition ($n = 1$ to 2), E_{RS} is the resonance energy in the rest frame,

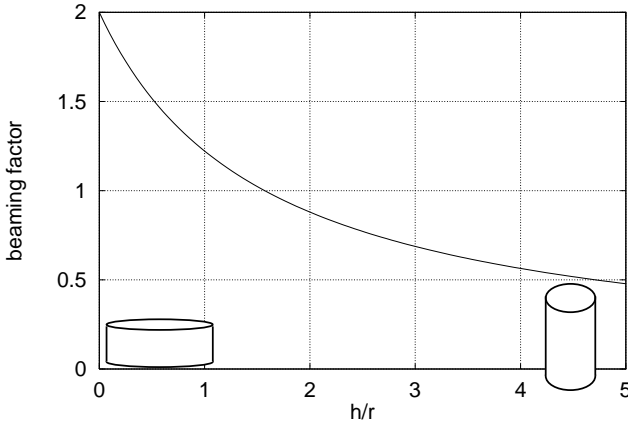


Figure B1. The collimation factor of geometrical beaming. The flux at $\theta = 0$ to the averaged flux [equation (B2)].

and ΔE is a resonance energy width [eq. (10.70) in Rybicki & Lightman 1979]. Numerically, the first factor is $\frac{\pi e^2}{m_{\text{Fe}} c} f_{12} = 1.2 \times 10^{-17} \text{ cm}^{-3}$, and the energy width ΔE in the second factor of Gaussian is determined by equations (5) and (6). Then, the cross section of resonance scattering at the line-center energy is given as

$$\sigma_{\text{RS}} = 2.0 \times 10^{-18} \left(\frac{E_0}{6.695 \text{ keV}} \right) \left(\frac{kT}{16 \text{ keV}} \right)^{-1/2} \text{ cm}^2. \quad (\text{A10})$$

APPENDIX B: GEOMETRICAL BEAMING IN THE ACCRETION COLUMN

How much enhancement can we expect in “geometrical beaming” in the accretion column (see §2.1)? Consider the case that the resonance line photons can only escape from the surface of the column. The directional photon flux emerging from the column is given as

$$f(\theta) d\cos\theta \propto \pi r^2 \cos\theta + 2rh \sin\theta, \quad (\text{B1})$$

where θ is the angle measured from the column axis. Therefore, the flux along $\theta \simeq 0$ is enhanced by a factor

$$\frac{f(\theta)}{\langle f \rangle} = \frac{\pi r^2}{\frac{1}{2}\pi r^2 + \frac{\pi}{2}rh} = \frac{2}{1 + \frac{2}{\pi} \left(\frac{h}{r} \right)}, \quad (\text{B2})$$

where $\langle f \rangle$ is the average of $f(\theta)$ over θ . At the coin-shaped limit ($\frac{h}{r} \rightarrow 0$), this factor approaches 2 (figure B1).

REFERENCES

Aizu, K. 1973, Prog. Theor. Phys., 49, 1184
 Bailey, J., Axon, D. J., Hough, J. H., Watts, D. J., Giles, A. B., Greenhill, J. G. 1983, MNRAS, 205, 1
 Bailey, J., Wickramasinghe, D. T., Hough, J. H., Cropper, M. 1988, MNRAS, 234, 19
 Beardmore, A. P., Ramsay, G., Osborne, J. P., Mason, K. O., Nosek, J. A., Baluta, C. 1995, MNRAS, 273, 742
 Beuermann, K., Thomas, H. -, Giommi, P., Tagliaferri, G. and Schwone, A. D. 1989, A&A, 219, 7
 Burke, B.E., Mountain, R.W., Daniels, P.J., Cooper, M.J., Dolat, V.S. 1994, IEEE Trans. Nucl. Sci., NS-41, 375

Burwitz, V., Reinsch, K., Schwone, A. D., Hakala, P. J., Beuermann, K., Rousseau, T., Thomas, H. -, Gansicke, B. T., Pirola, V., Vilhu, O. 1998, A&A, 331, 262
 Catalán, M. S. and Schwone, A. D. and Smith, R. C. 1999, MNRAS, 310, 123
 Cropper, M. 1990, SSRv, 54, 195
 Done, C., Osborne, J. P., Beardmore, A. P. 1995, MNRAS, 276, 483
 Done, C. Osborne, J. P. 1997, MNRAS, 288, 649
 Done, C. Magdziarz, P. 1998, MNRAS, 298, 737
 Ezuka, H., Ishida, M. 1999, ApJS, 120, 277
 Ferrario, L., Wickramasinghe, D. T., Bailey, J., Tuohy, I. R., Hough, J. H. 1989, ApJ, 337, 832
 Fujimoto, R., Ishida, M. 1997, ApJ, 474, 774
 Greiner, J., Remillard, R. A., Motch, C. 1998, A&A, 336, 191
 Harrop-Allin, M. K., Cropper, M., Potter, S. B., Dhillon, V. S., Howell, S. B. 1997, MNRAS, 288, 1033
 Hoshi, R. 1973, Prog. Theor. Phys., 49, 776
 Ishida, M. 1991, Ph.D. thesis, Univ. of Tokyo
 Ishida, M., Matsuzaki, K., Fujimoto, R., Mukai, K., Osborne, J. P., 1997, MNRAS, 287, 651
 Ishida, M., Greiner, J., Remillard, R. A., Motch, C., 1998, A&A, 336, 200
 Makishima, K., Tashiro, M., Ebisawa, K., Ezawa, H., Fukazawa, Y., Gunji, S., Hirayama, M., Idesawa, E., Ikebe, Y., Ishida, M., Ishisaki, Y., Iyomoto, N., Kamae, T., Kaneda, H., Kikuchi, K., Kohmura, Y., Kubo, H., Matsushita, K., Matsuzaki, K., Mihara, T., Nakagawa, K., Ohashi, T., Saito, Y., Sekimoto, Y., Takahashi, T., Tamura, T., Tsuru, T., Ueda, Y., Yamasaki, N. Y. 1996, PASJ, 48, 171
 Mewe, R., Gronenschild, E. H. B. M., van den Oord, G. H. J. 1985, A&AS, 62, 197
 Misaki, K., Terashima, Y., Kamata, Y., Ishida, M., Kunieda, H., Tawara, Y. 1996, ApJ, 470, 53
 Norton, A. J., Watson, M. G. 1989, MNRAS, 237, 853
 Ohashi, T., Ebisawa, K., Fukazawa, Y., Hiyoshi, K., Horii, M., Ikebe, Y., Ikeda, H., Inoue, H., Ishida, M., Ishisaki, Y., Ishizuka, T., Kamijo, S., Kaneda, H., Kohmura, Y., Makishima, K., Mihara, T., Tashiro, M., Murakami, T., Shoumura, R., Tanaka, Y., Ueda, Y., Taguchi, K., Tsuru, T., Takeshima, T. 1996, PASJ, 48, 1570
 Rybicki, G.B. & Lightman, A.P. 1979, Radiative Processes in Astrophysics (New York: Wiley)
 Schwone, A. D., Catalán, M. S., Beuermann, K., Metzner, A. ;, Smith, R. C., Steeghs, D. 2000, MNRAS, 313, 533
 Spitzer, L. 1962, Physics of Fully Ionized Gases (New York: Wiley)
 Terada, Y., Kaneda, H., Makishima, K., Ishida, M., Matsuzaki, K., Nagase, F., Kotani, T. 1999, PASJ, 51, 39
 Thomas, H. -, Reinsch, K. 1996, A&A, 315L, 1
 Schwone, A. D., Thomas, H. -, Beuermann, K., Reinsch, K. 1993, A&A, 267, 103
 Serlemitsos, P. J., Jalota, L., Soong, Y., Kunieda, H., Tawara, Y., Tsusaka, Y., Suzuki, H., Sakima, Y., Yamazaki, T., Yoshioka, H., Furuzawa, A., Yamashita, K., Awaki, H., Itoh, M., Ogasaka, Y., Honda, H., Uchibori, Y. 1995, PASJ, 47, 105
 Szkody, P., Vennes, S. ;, Schmidt, G. D., Wagner, R. M., Fried, R., Shafter, A. W., Fierce, E. 1999, ApJ, 520, 841
 Wickramasinghe, D. T., Bailey, J., Meggitt, S. M. A., Ferrario, L., Hough, J., Tuohy, I. R. 1991, MNRAS, 251, 28
 Wu, K., Chanmugam, G., Shaviv, G. 1995, ApJ, 455, 260
 Yamashita, A., Dotani, T., Bautz, M., Crew, G., Ezuka, H., Gendreau, K., Kotani, T., Mitsuda, K., Otani, C., Rasmussen, A., Ricker, G., Tsunemi, H. 1997, IEEE Trans. Nucl. Sci., NS-44, 847